International Conference on Space Optics—ICSO 2022

Dubrovnik, Croatia

3–7 October 2022

Edited by Kyriaki Minoglou, Nikos Karafolas, and Bruno Cugny,

ICSO 2022
International Conference on Space Optics
3 – 7 October 2022 | Dubrovnik | Croatia

An autonomous and passive daytime air-turbulence monitor for FSOC link optimization

icso proceedings

International Conference on Space Optics — ICSO 2022, edited by Kyriaki Minoglou, Nikos Karafolas,
Bruno Cugny, Proc. of SPIE Vol. 12777, 127775N · © 2023 ESA and CNES · 0277-786X · doi: 10.1117/12.2691033

An autonomous and passive daytime air-turbulence monitor for FSOC link optimization

Maxime Lamotte, author[a] and Frédéric Jabet, co-author[a]

[a]Miratlas, 139 Rue De Girard, F84120 Pertuis, France

ABSTRACT

In the advent of Free-Space Optical Communications, laser links between feeder stations and satellites are foreseen to surpass radiofrequency (RF) in terms on low-latency, high bandwidth and reliable security thanks to a narrow angle of emission and possibility en encrypt communications with quantum keys. Because Earth's atmosphere is subject to wind and temperature gradients, turbulence skews laser beams over divergent and random paths, eventually corrected with Adaptive Optics (AO). Demonstrators have shown need for gateway selection optimization based on turbulence monitoring, to reduce onboard telescope re-pointing manoeuvrers, link-power budget, data errors correction and handover times. To assess day-time atmosphere optical quality, Miratlas has developed an autonomous and passive daytime turbulence monitor based on sunlight scintillation. This so-called SHAdow BAnd Ranger (SHABAR) was designed with remote-site prospective analysis requirements as well as operational feeder station monitor. Design of this small footprint, durable and low-cost device is presented, along a preliminary result campaign obtained at various locations. Power-spectral densities and autocorrelations of sunlight scintillation showed a clear effect of lower atmosphere wind gusts, while higher-layers also produced low-frequency scintillation. Air refractive-index structure parameter, $C_N^2(h)$ obtained from such scintillation measurements is presented. A Machine-Learning algorithm, fed by numerous environmental sensors embedded in our Integrated Sky Monitor (ISM) is foreseen to offer short-time turbulence prediction. Further experimental campaigns at reference site with calibrated instruments is expected later this year for commissioning of our turbulence profiler.

Keywords: Free-Space Optical Communications, Turbulence monitoring, Cn2, Teleport

1. INTRODUCTION

Free-Space Optical Communications (FSOC) are foreseen to be the keystone of tomorrow's fast, secure and low-latency worldwide data connection. Early demonstrators and commercial satellite fleets are currently being developed by several space agencies and industrial actors. Most of today's development plans include a unique active feeder link aiming at a geostationary orbiting satellite (GEO) to avoid extra mechanical pointing challenges. Ground to satellite optical link requires knowledge of cloud coverage, absorption and turbulence to estimate a power budget, available bandwidth and an optimized data routing plan. If bad atmospheric conditions above active feeder degrades link's quality, another feeder gateway, located 100's of kilometres away with better parameters may be selected and a latency-free handover is triggered.
Of the 3 aforementioned predominant phenomena in optical link quality degradation, turbulence is the less apparent but has a significant impact: a clear sky does not necessarily translates into a good optical propagation medium. Two major effects are produced by turbulence;

Beam spreading is the widening of optical beam due to diffraction on turbulent eddies smaller than the beam waist. Such phenomena does not deviates the propagation path but increased the PSF, energy is spread over a larger area.

Further author information: (Send correspondence to M.L.)
M.L.: E-mail: mlamotte@miratlas.com
F.J.: E-mail: fjabet@miratlas.com

Beam wandering is the deviation of optical beam due to refraction on turbulent eddies larger than the beam waist. Large convection cells induce step-index changes along great propagation distances, such as a GEO link. The laser beam is deviated from its aimed path.

Fig.1 proposes a representation of these effects, on a theoretical ground-to-GEO optical link.
Turbulence profile can be measured by bulky, expensive and active apparatus, such as radiosounding, LIDAR, SODAR or instrumented towers. For site-selection and feeder station monitoring, we focused on a small, rugged, maintenance-free and low cost turbulence-profiler, as expected by telecom operators to probe a myriad of prospective locations without civil work.

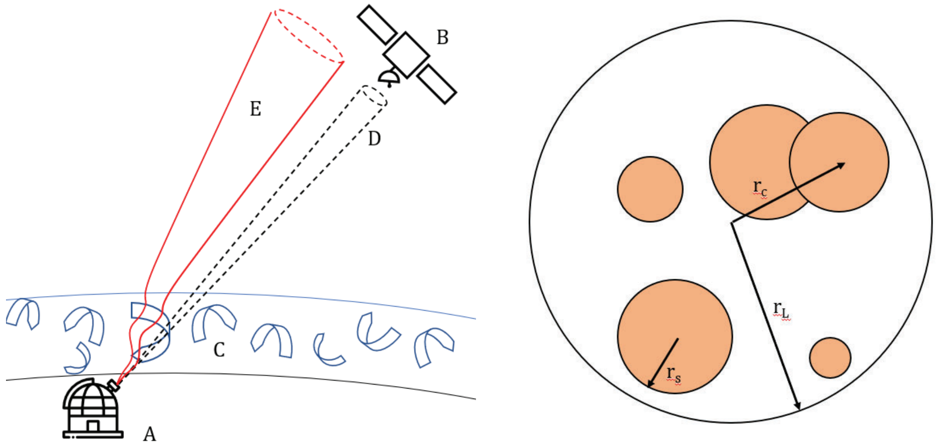

Figure 1: (Left) Beam-spreading mechanisms encountered by an FSOC link. A feeder station A aiming at satellite B through atmosphere C would have a narrow and aimed beam D without turbulence. Real eddies in both low and high altitude layers induce beam spreading and deviation E, challenging link quality.
(Right) Representation of the real optical beam at satellite altitude. Speckles of radius R_s located at R_c from the theoretical centre may be observed, and all light might be ducted within radius R_L.

The SHAdow BAnd Ranger (SHABAR) is a well-acknowledged device for probing ground-layer turbulence profile during daytime, up to about a kilometre high. Several SHABAR have been employed for solar observatory site selection[1],[2] daylight seeing monitoring[3] and lower-layer turbulence characterization[4][5][6] . Some devices, generically named LuSci, rely on the Moon scintillation to retrieve $C_N^2(h)$ profile at night, they can be a future evolution of our device.
Prediction of atmospheric conditions over different ground stations for network planning is foreseen to be achievable through Machine Learning (ML) of large atmospheric databanks collected on-site by tens of sensors. Such ML-generated turbulence prediction based on previous records and large environmental databanks has already been tested on an astronomical observatory.[7] Compact and rugged night turbulence monitor (C-DIMM), along with a day Sky-Scintillation Monitor (SSM) to retrieve Fried's parameter are parts of our Integrated Sky Monitor (ISM), previously designed by Miratlas[8] and operated by several research institutes. In our endeavour for reliable network planning and optical link quality optimization, we developed an autonomous daytime turbulence monitor probing sunlight's scintillation to estimate local atmospheric refractive index structure parameter, commonly referred as $C_N^2(h)$.

In this paper, we will recall a short presentation of SHABAR's work principle and applications in Sec.2. Our device development in the scope of FSOC will be described in Sec.3. Early results from 3 different locations will be assessed and commented in Sec.4.

2. SHABAR PRINCIPLE

Scintillation of starlight has long been employed as a quantitative measure of night seeing by astronomers. Because stars are ideal infinitely small emission points, their resulting scintillation index during high-altitude windy nights, can reach up to complete extinction due to beam wandering. Observation of stars' point spread function (PSF) remains today's easiest way to measure night-time seeing.

During day-time, only the Sun may be used as a remote light source, but its large, finite diameter (about 960 arcsec) lead to significantly lower scintillation index, detectable with finely tuned electronics.

Seykora[9] concluded that Sun scintillation on a single pupil detector at Sacremento Peak observatory can be correlated to picture quality and, in fine, Fried's parameter r_0. Beckers[10] proposed an expression to link solar scintillation σ_i^2 to $C_N^2(h)$ using Roddier[11] theory.

$$\sigma_i^2 = 20 \cdot \Omega^{-7/3} \cdot \cos^{-2/3} \cdot\zeta \int_0^{\infty} dh \cdot h^{-1/3}\, C_N^2(h) \tag{1}$$

where d is detector's diameter, Ω is Sun's diameter in radians, σ_i is irradiance fluctuation and h is observed layer's height, ζ is the zenith distance.

On a single-aperture detector, only an integrated r_0 value, Fried's parameter, can be determined. It is linked to $C_N^2(h)$ by the following[2] expression:

$$r_0(h) = 0.18466 \cdot \lambda^{6/5} \cdot \sec^{3/5} \cdot\zeta \left[\int_h^{\infty} C_n^2(h)\, dh\right]^{-3/5} \tag{2}$$

Later, Beckers et al.[12] reported the decreasing covariance of Sun's scintillation, at ranging scintillometer spacing along a baseline. Fields of views of such detectors being strictly equal, different heights can be simultaneously probed for scintillation, hence outputting direct information on $C_N^2(h)$ structure function.

A schematic of basic SHABAR principle and geometry is depicted in Fig.2.

Inversion of covariance data to retrieve an estimated $C_N^2(h)$ profile requires a computer-intensive procedure, as detailed in.[2] To improve computing efficiency and reduce our system's latencies and power consumption, we coded routines into a parallel Python 3 language.

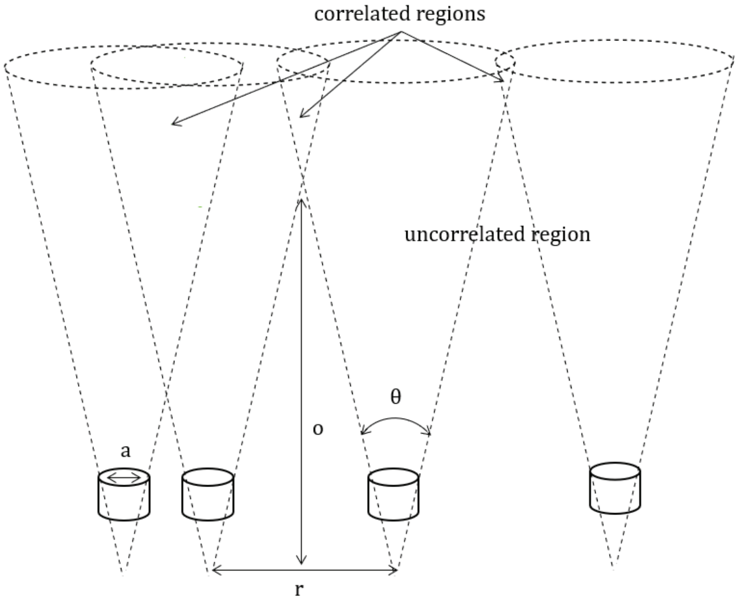

Figure 2: SHABAR principle: a baseline of scintillometers of diameter a is spaced evenly by length r. Measurements at height o display correlations as regions are being simultaneously probed.

3. DESIGN

A typical so-called ”short-baseline” SHABAR consists of 6 scintillometers evenly placed into a sub-50cm long profiled aluminium beam. The U-shape of such beam ensures a high planar second moment of area, and reduces possible wind-induced vibrations, possibly detected as scintillation. The ”detection-beam” is bolted on a dedicated az-alt mount designed for extreme weather conditions, water ingress protection and impact tolerance. Unlike other authors,[3] we did not synchronized the tracking mount with a dedicated Sun-looking camera but to align roughly the tracker, as scintillometers' large field of view tolerates misalignment of several degrees. Less than 50 W of installed power are necessary to run the tracker, instrumentation, computer and accessories. Between 2 movements of the tracker, each 10 seconds, power consumption is kept below 20 W so our SHABAR can run on solar-panels at remote locations.
Raw and inverted data can be stored locally or sent over line-network (LAN). We also set-up a LTE-backed SHABAR so several inaccessible assessed places can be benchmarked in real-time.

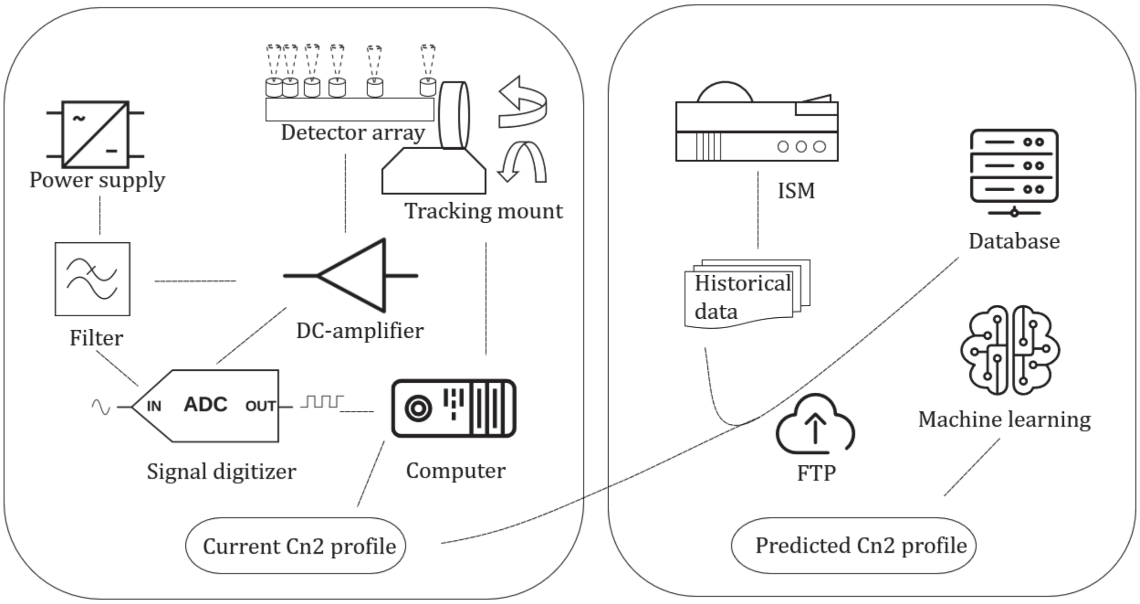

Figure 3: (Left) Main components of the turbulence profiler system, to retrieve a current $C_N^2(h)$ with onboard computational power. (Right) External devices, data and protocol employed for short-time atmospheric turbulence forecast.

3.1 Scintillation detection

Most SHABAR and LuSci devices relies on AC-coupled signal amplification and acquisition. Reliance on such configuration allows for high gains (ie: 1920 for Seykora et al.[10]) obtained various daisy-chained amplifiers, but also increase noise in the resulting digitized signal. Extreme weather conditions to be found at test facilities implies dramatic changes on capacitor and resistor values, even with low-temperature-drift components, biasing filter and amplifier responses. Finally, AC-coupling distorts and cuts-off very low frequencies that could be taken into account for upper-atmosphere characterization. For all these reasons, we decided, as previously done by Pfrommer et al.[13] to implement a DC-coupled scintillometer baseline. By digitizing the whole, low-amplified signal on a high-precision Analog-to-Digital converter (ADC), we aim at performing an almost full-numerical filtering and amplification for a drift-less acquisition.
Doing so challenges our acquisition chain noise performance, as Tokovinin et al.[14] reported on a LuSci. Grounding, shielding of a transimpedance amplifier (TIA) and use of a quality ADC were also previously reported to be crucial for viability of DC-coupling system. Nethertheless, recent studies, from Hale et al.[15] showed promising

results for upper-atmosphere dust clouds measurements, and Sunlight extinction with a DC-coupled scintillometer.

A quartz-windowed and metal-encased photodiode, with a 1mm^2 active area has been chosen given its excellent Noise Equivalent Performance (NEP), around 1E-15 W/$\sqrt{\text{Hz}}$. Unlike previous implementations, we chose to rely on small-area detectors, as they display lower capacitance and eventually better higher-frequency response if no bias is applied between their electrodes. Photovoltaic mode, also called zero-bias, is preferred for low-frequency and high sensitivity applications because of a lower dark-current. On a typical Sun scintillation, no frequencies above 10 kHz are expected.

The self-developed TIA is built around a recent low-noise amplifier chip, reaching input voltage noise below 6 nV/$\sqrt{\text{Hz}}$. The TIA outputs a noiseless 3 V voltage when photodiodes are illuminated with a 532 nm, stabilized laser having an similar luminous flux as the Sun at zenith on a clear day. Overall, we concluded our acquisition chain had a Signal-to-Noise ratio above 120 dB, our spectrum-analyser detection limit.

3.2 Tracking mount

A reliable, low-voltage and heavy-duty tracking mount is required for shipping, quick installation and harsh-environment operation over several months. We sourced and modified az-alt mount relying on high-ratio straight-gears and step-motors. Such mechanical assembly can sustain a 10 kg payload and display a 1 deg pointing precision on both axis. Position feedback is monitored via the sent step-motors pulses and is reset at each homing thanks to dead-end switches. Upon selection for production, the tracking mounts were exposed to direct Sunlight, UV-radiation, high-pressure water jets and condensing atmosphere during a week.

Communication with the tracking mount is ensured by an embedded low-power micro-computer, generating a Graphical User Interface (GUI) for control, data output and maintenance procedures, as seen on Fig.4 . Because we do not include a Sun-tracking camera to save on computation power, a Network Time Protocol (NTP) is called every day, and checked against a battery-backed-up Real-Time Clock (RTC) module. Sun's position is computed and updated every 10 seconds to lower vibration signals on the photodiodes.

Wind Profiler Control

Measured position
92.7
22.7

Computed position
91.79
21.9

Manual tracking
Estimated Sun power 642.7
On-board UTC Up to date
Last acquisition VALID
Time awaken 2d 15h 45m
Spare label

0.0 Target Azimuth
0.0 Target Altitude

Zulu RTC time
6 49 54

○ Auto tracking
● Manual tracking
☑ Record data

Figure 4: Remote-desktop view of our SHABAR GUI for tracking-mount control and real-time data viewing. The last acquisition covariance plot is visible at the bottom.

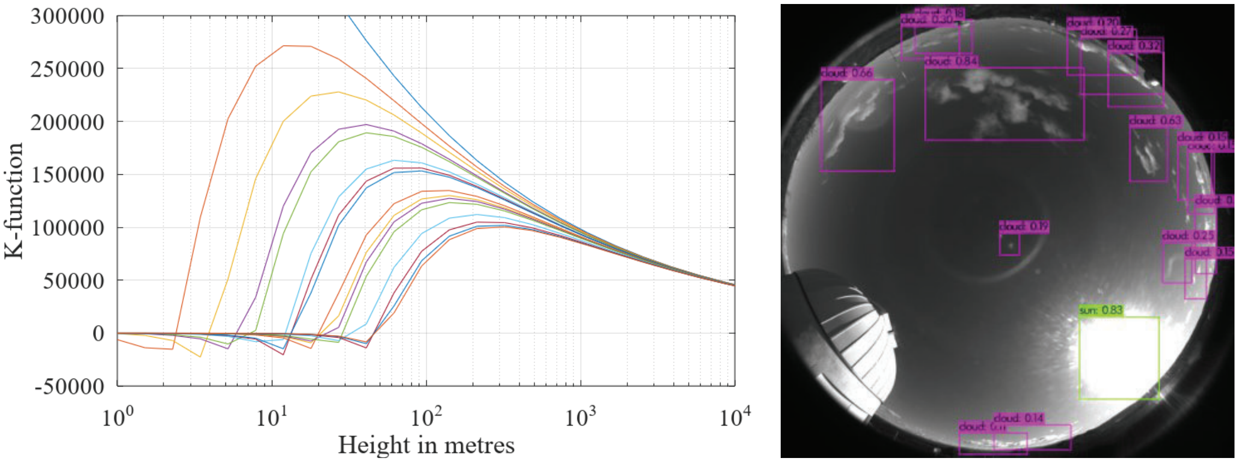

(a) Kernel function for inversion procedure. Large initial overshoot is induced by small detector aperture.

(b) ML-generated cloud detection for flagging validity of scintillation measurements.

Figure 5: Kernel function and cloud-identification algorithm used for data inversion.

3.3 Inversion procedure

From $C_N^2(h)$, one can estimate Fried's parameter r_0, isoplanatic angle θ_0 and atmospheric timescale τ_0. Night-time wind and index-of-refraction fluctuations with altitude are well defined by semi-empirical equations, but day-time profiles are somewhat more challenging, due to ground-heating induced convection.

Inversion procedures were written in Python3 language for its ability to produce quality graphs, variety of signal-processing library and a short development time. A simplified yet straightforward description of Hill et al. theory is described in Sliepen et al. paper.[3]

Before processing inversion, raw data are digitally filtered to reject any unusable dataset. Theoretical Sunlight power is checked against each scintillometer response so defective or stained cells can be detected and discarded. Clouds, even thin cirrus, would skew a computed turbulence profile, are therefore checked against theoretical received power. If an ISM is located by the SHABAR, a ML algorithm detects clouds in the Sun vicinity and sets a rejection flag on the last dataset.

If latest acquisition appear to be valid, it is pushed by secured-FTP to a local ISM for inversion procedure where it can be treated online or by batch. Resultant estimated $C_N^2(h)$ profile is saved as a lightweight dataset, eventually shown locally on the GUI. To ease convergence of the final Amoeba algorithm, we set-up a ground-layer modified Huffnagel-Valley 5/7 $C_N^2(h)$ profile as initial guess. A single 30 s long scintillometer dataset is inverted in 10 seconds, allowing uninterrupted turbulence monitoring.

4. EARLY RESULTS

4.1 Raw data analysis

After an extensive testing of electronic boards to ensure a noiseless data acquisition, a single scintillometer unit was set-up outside during winter 2022. Strong winds in lower and higher layers (Mistral wind), assorted with clear skies were assessed to tweak and optimize the acquisition chain in terms of amplifier and ADC bandwidth. As a last commissioning test, 6 scintillometers were set up in an electromagnetic (EM) shielded enclosure, without tracking mount, to assess possible EM-noise ingress over coaxial cables and TIA in the final SHABAR design. This shielded unit was powered with a 14.8 V Li-Po battery without active regulator, and data were collected on a personal computer powered on its battery. TIA supply voltage, dark and laser-illuminated scintillator signals shown a standard deviation of less than an 1 ADU on each channel, this corresponds to a solar scintillation signal σ_i of 6.62`E`-5, on a 5 V scale. No discrepancies between the 2 configurations were found, and our first batch SHABAR was declared usable.

Tab.1 sums-up datasets to be shown in the following section.

Figure 6: (Left) SHABAR prototype at dawn by Saint-Véran observatory site, 3000 m high.
(Right) Close-up view of the SHABAR prototype, installed on our office roof. All instrumentation is embedded in the rear water-tight enclosure.

Table 1: Dataset analysed in this publication.

Dataset	Conditions
AQ1	Dark signal of a standard SHABAR
AQ2	Winter morning clear sky on city roof with strong wind gusts at ground layer
AQ3	Winter morning clear sky on city roof with high constant altitude wind
AQ4	Summer noon on city roof during heatwave, no wind at ground height
AQ5	Summer noon at 3000 m at observatory site, no wind at ground height

Fig.7 displays a typical Power Spectrum Density (PSD) obtained on 10000 Hanning windows when low-altitude wind is blowing (left) or not (right) at ground layer. If strong wind gusts of convection are encountered, scintillation power spectra display a clear increase in higher frequencies signal strengths. Steep decrease visible on the rightmost part of Fig.7a reach up to 12 dB/decade, but the ”tipping point” with a 1/f noise signal on the leftmost part, seems to vary consequently with lower-layer turbulences.

Plotting autocorrelation of the same data, Fig.7b, reveals clear and straight structures, coherent with a slowly-varying envelope signal. Conversely, scintillations observed under wind gusts or strong convection due to intense Sunlight on a dark roof induce a lower, if any, autocorrelation curve.

On Fig.8, moving-mean averaged Sunlight intensities were plotted on 2 extremes cases, namely AQ2 and AQ5, to identify low-frequency patterns. Smoothing is operated on a 500 ms segment on each of the 6 photocells to show similarities and lag.

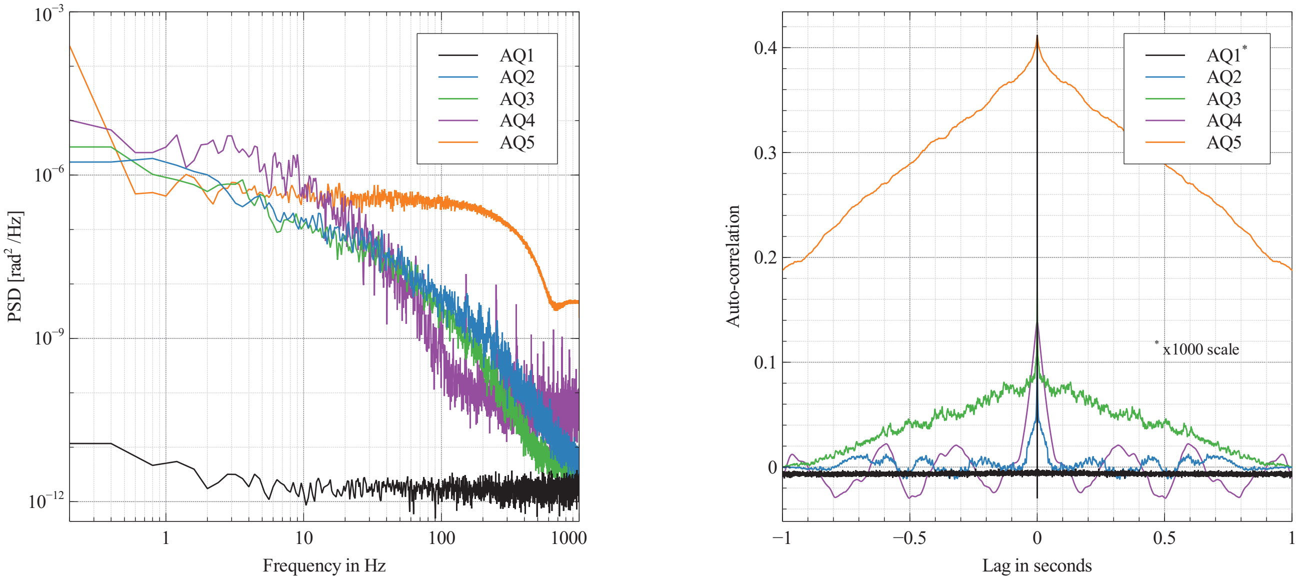

(a) PSD of a single scintillometer unit, 30 s long. (b) Autocorrelations of the very same scintillometers.

Figure 7: PSD and autocorrelation of scintillometer number 3, at different places and time

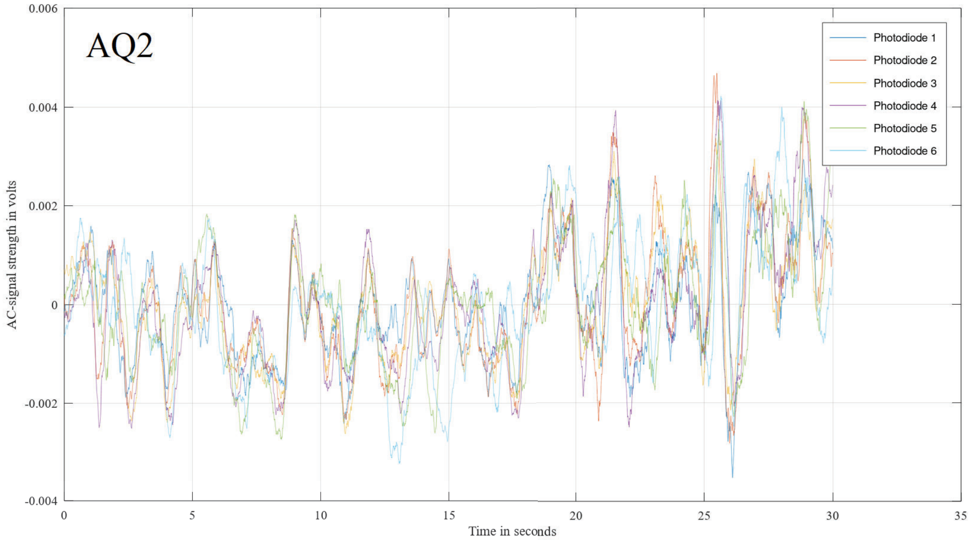

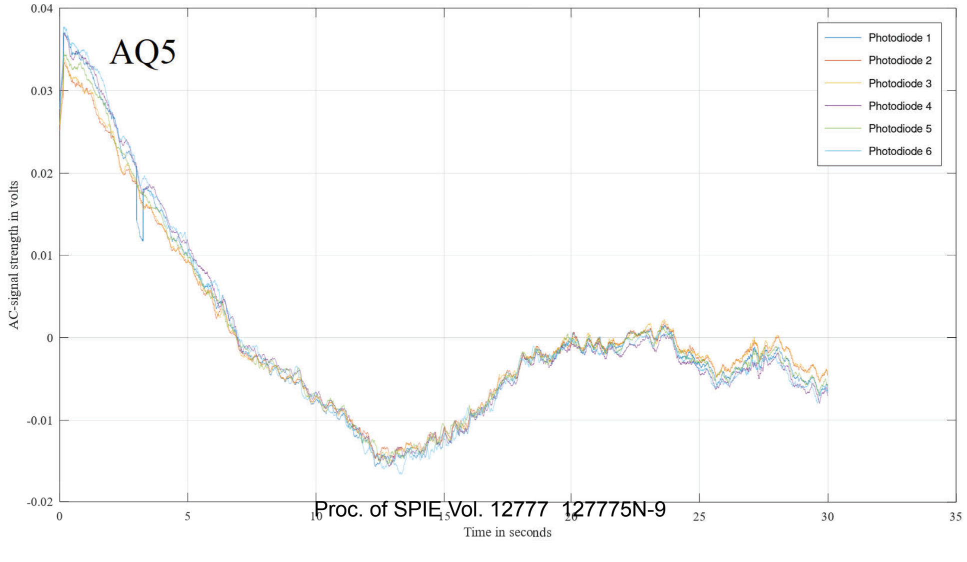

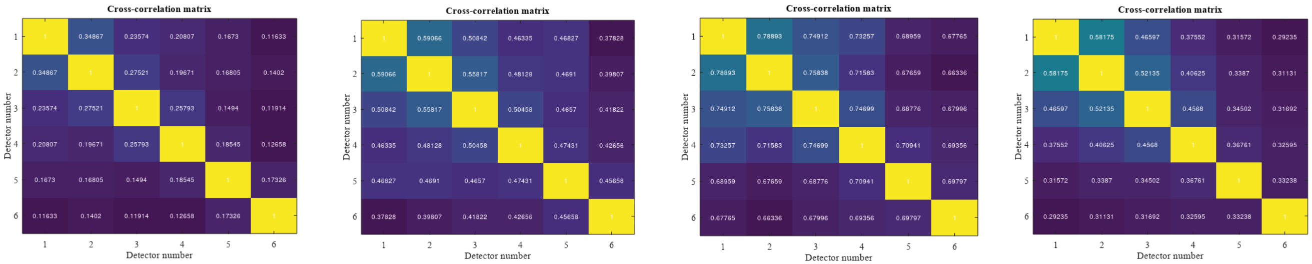

Cross-correlation matrix

Detector number	1	2	3	4	5	6
1	1	0.34867	0.23574	0.20807	0.1673	0.11633
2	0.34867	1	0.27521	0.19671	0.16805	0.1402
3	0.23574	0.27521	1	0.25793	0.1494	0.11914
4	0.20807	0.19671	0.25793	1	0.18545	0.12658
5	0.1673	0.16805	0.1494	0.18545	1	0.17326
6	0.11633	0.1402	0.11914	0.12658	0.17326	1

Cross-correlation matrix

Detector number	1	2	3	4	5	6
1	1	0.59066	0.50842	0.46335	0.46827	0.37828
2	0.59066	1	0.55817	0.48128	0.4691	0.39807
3	0.50842	0.55817	1	0.50458	0.4657	0.41822
4	0.46335	0.48128	0.50458	1	0.47431	0.42656
5	0.46827	0.4691	0.4657	0.47431	1	0.45658
6	0.37828	0.39807	0.41822	0.42656	0.45658	1

Cross-correlation matrix

Detector number	1	2	3	4	5	6
1	1	0.78893	0.74912	0.73257	0.68959	0.67765
2	0.78893	1	0.75838	0.71583	0.67659	0.66336
3	0.74912	0.75838	1	0.74699	0.68776	0.67996
4	0.73257	0.71583	0.74699	1	0.70941	0.69356
5	0.68959	0.67659	0.68776	0.70941	1	0.69797
6	0.67765	0.66336	0.67996	0.69356	0.69797	1

Cross-correlation matrix

Detector number	1	2	3	4	5	6
1	1	0.58175	0.46597	0.37552	0.31572	0.29235
2	0.58175	1	0.52135	0.40625	0.3387	0.31131
3	0.46597	0.52135	1	0.4568	0.34502	0.31692
4	0.37552	0.40625	0.4568	1	0.36761	0.32595
5	0.31572	0.3387	0.34502	0.36761	1	0.33238
6	0.29235	0.31131	0.31692	0.32595	0.33238	1

Figure 9: Correlation matrices of the 6 scintillometers, during 4 acquisitions at Saint-Véran observatory site.

Large low-frequency oscillations of Fig.8(up), with a ≈ 1 s period envelop smaller, high-frequency signal variations, smoothed by the moving-mean filter. Under a pristine sky, with r_0 reaching 20 cm on Fig.8(down), the strong coherence between each photodiode signal is visible, but the large signal fluctuation in the mHz range is tracked thanks to DC-coupling and filter-less acquisition system.

4.2 Cn2 profile restoration

Correlation coefficients between each detector time-series are displayed Fig.9 for four acquisitions separated by 10 minutes, on a summer noon at Saint-Véran observatory.
A single, direct output $C_N^2(h)$ profiles, over 30 s long period is presented on Fig.10. This plot was obtained using a modified version of the algorithm of Hill et al.[2] Because SHABAR devices are blind above 1000 m of height, as mentioned on Fig.5a, upper estimation of $C_N^2(h)$ is expected to follow a Hufnagel-Valley profile modified for day-time conditions.

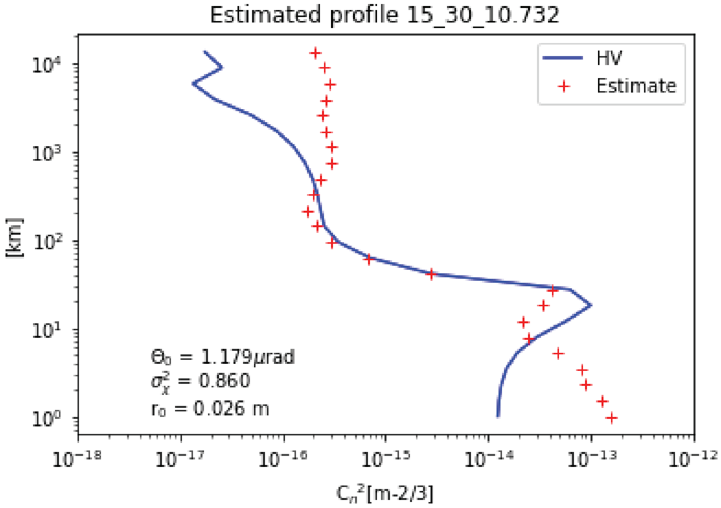

Figure 10: $C_N^2(h)$ profile generated from Sun scintillation measurements on acquisition AQ3.

5. CONCLUSION

A day-time turbulence profiler has been designed and field-tested in the frame of Free-Space Optical Communications (FSOC). Its passive, low-power and autonomous operation targets remote-location probing for site-selection and data routing optimization. $C_N^2(h)$ profiles up to 1000 m heights are obtained with direct measurements, while upper altitudes profiles may be determined by analytical means, checked against integrated r_0 values. A validation campaign on different test-sites equipped with radio-sounding, LIDAR and instrumented tower is forecasted prior commissioning on possible future teleport locations.

REFERENCES

[1] Socas-Navarro, H., Beckers, J., Brandt, P., Briggs, J., Brown, T., Brown, W., Collados, M., Denker, C., Fletcher, S., Hegwer, S., et al., "Solar site survey for the advanced technology solar telescope. i. analysis of the seeing data," *Publications of the Astronomical Society of the Pacific* **117**(837), 1296 (2005).

[2] Hill, F., Radick, R., and Collados, M., "Deriving c2 n (h) from a scintillometer array," *ATST Site Survey Working Group Final Report. ATST Proj. Doc* **14** (2003).

[3] Sliepen, G., Jägers, A. P., Bettonvil, F. C., and Hammerschlag, R. H., "Seeing measurements with autonomous, short-baseline shadow band rangers," in [*Ground-based and Airborne Telescopes III*], **7733**, 1586–1596, SPIE (2010).

[4] Hickson, P., Gagné, R., Pfrommer, T., and Steinbring, E., "Astronomical seeing and ground-layer turbulence in the canadian high arctic," *Monthly Notices of the Royal Astronomical Society* **433**(1), 307–312 (2013).

[5] Hickson, P., Carlberg, R., Gagne, R., Pfrommer, T., Racine, R., Schöck, M., Steinbring, E., and Travouillon, T., "Boundary layer seeing measurements in the canadian high arctic," in [*Ground-based and Airborne Telescopes III*], **7733**, 636–646, SPIE (2010).

[6] Hickson, P. and Lanzetta, K., "Measuring atmospheric turbulence with a lunar scintillometer array," *Publications of the Astronomical Society of the Pacific* **116**(826), 1143 (2004).

[7] Gilda, S., Ting, Y.-S., Withington, K., Wilson, M., Prunet, S., Mahoney, W., Fabbro, S., Draper, S. C., and Sheinis, A., "Astronomical image quality prediction based on environmental and telescope operating conditions," *arXiv preprint arXiv:2011.03132* (2020).

[8] Jabet, F., "C-dimm: an autonomous, outdoor and fixed seeing monitor for astronomy, atmospheric studies and free space optical communications," in [*Environmental Effects on Light Propagation and Adaptive Systems IV*], **11860**, 6–10, SPIE (2021).

[9] Seykora, E., "Solar scintillation and the monitoring of solar seeing," *Solar Physics* **145**(2), 389–397 (1993).

[10] Beckers, J. M., "On the relation between scintillation and seeing observations of extended objects," *Solar Physics* **145**(2), 399–402 (1993).

[11] Roddier, F., "V the effects of atmospheric turbulence in optical astronomy," in [*Progress in optics*], **19**, 281–376, Elsevier (1981).

[12] Beckers, J. M., Leon, E., Mason, J., and Wilkins, L., "Solar scintillometry: calibration of signals and its use for seeing measurements," *Solar Physics* **176**(1), 23–36 (1997).

[13] Pfrommer, T. and Hickson, P., "High-resolution ground layer turbulence from inside the cfht dome using a lunar scintillometer," in [*Journal of Physics: Conference Series*], **595**(1), 012027, IOP Publishing (2015).

[14] Tokovinin, A., Bustos, E., and Berdja, A., "Near-ground turbulence profiles from lunar scintillometer," *Monthly Notices of the Royal Astronomical Society* **404**(3), 1186–1196 (2010).

[15] Hale, S., Chaplin, W., Davies, G., Elsworth, Y., Howe, R., and Pallé, P., "Measurement of atmospheric scintillation during a period of saharan dust (calima) at observatorio del teide, izãna, tenerife, and the impact on photometric exposure times," *Publications of the Astronomical Society of the Pacific* **132**(1009), 034501 (2020).